Development of a multi-species transport space theory and its application to permeation behavior in proton-conducting doped perovskites†

Michael Sanders and Ryan O'Hayre*

This paper examines the multi-species (simultaneous proton, oxygen vacancy, and electron/electron hole) transport behavior of proton conducting oxides. Multi-species transport behavior broadens both the realm of applications and also the potential challenges for the technical use of these perovskite materials in devices such as fuel cells, separation membranes, and membrane reactors. In order to better understand the interplay between the various transporting species and their impact on macroscale conduction and permeation processes, a new conceptualization of multi-species transport is proposed. A general theoretical description of multi-species transport is presented in a graphical manner that is similar to a ternary phase diagram. When combined with data gathered from water isotope permeation experiments, we show that it is possible to specify the relative contributions from each mobile defect species in a yttria-doped barium zirconate multi-species perovskite transport membrane system under a variety of experimental conditions. This approach provides a unique method to obtain and analyze transport behavior on the basis of transference numbers, thereby providing information which is often difficult to determine by other means.

1 Introduction

Proton conducting ceramics have been of great scientific interest since their initial development nearly 30 years ago.[1] In that time, the ABO_3 perovskite family of materials has shown particularly significant promise and has thus been the subject of intense research. Nevertheless, gaps in the scientific understanding of these materials have hampered their deployment in technical applications such as intermediate-temperature fuel cells. One of the more interesting and yet understudied characteristics of these ceramics is their propensity to exhibit multi-species conduction behavior—specifically the simultaneous occurrence of protonic and oxygen vacancy conduction in addition to electronic (electron or hole) conductivity. An often overlooked extension of this multi-species transport is the prediction of steam permeation; the chemical transport of water across a fully dense perovskite membrane.

Multi-species conduction broadens both the realm of potential applications and also the potential challenges for the technical use of these perovskite materials. Applications that could harness these multi-species conduction effects include sensors, hydrogen and oxygen separation membranes,[2,3] membrane reactors,[2,4] and the chemical permeation of steam.[5] At the same time, however, multi-species ionic transport can also introduce limitations to the use of these perovskite materials as electrolytes in high-drain electrochemical devices such as fuel cells,[6–8] an area where they are currently seeing significant application. Some of the implications of multi-species participation on conduction and hydration behavior have recently been examined by Han-Ill Yoo and colleagues.[9,10]

The majority of the research performed to-date on proton conducting ceramic materials exhibits two common traits. Firstly, because the proton conducting aspect of these materials has been of primary interest, proton conductivity has been intensely investigated while the potential oxygen ion and electrical conductivity of these materials has sometimes been neglected. Secondly, transport studies have been conducted almost exclusively using conductivity measurements. The research presented here breaks from both of these trends. First, this paper presents a new conceptual framework which is designed to explicitly capture the multi-species transport behavior of these materials. Secondly, this paper employs experimental permeation measurements, rather than conductivity measurements, to explore the multi-species transport behavior of these materials systems in new ways. Unlike conductivity measurements, permeation experiments do not require the charge compensation or electric driving force supplied by electrodes. Permeation is electrode-less and therefore charge balance must be conserved internally during transport. This requirement *necessitates* multi-species transport coupling and accentuates minority carrier species, whereas conductivity measurements accentuate the majority carrier species. A further important feature of this permeation approach is that the various ionic transport species of interest in the system (namely O^{2-} and H^+) can be studied directly and separately using isotopically labeled tracers (such as ^{18}O and ^2H).

2 Theory

2.1 Multi-species permeation transport model

Because conductivity is the most frequently measured transport property in ionic and mixed ionic-electronic systems, most transport models are based on the assumption that an external

Colorado School of Mines, 1500 Illinois St, Golden, CO, USA. E-mail: rohayre@mines.edu; Tel: +303.273.3952

electrical potential drives transport. Considerably fewer multi-species transport models have considered permeation. In contrast to conduction, transport in permeation membranes is driven by gradients in chemical potential rather than external electrical potential. Furthermore, because charge compensation through external electrical conduction is absent in an electrode-free permeation cell, the additional constraint of constant electroneutrality is imposed on the transport system. This electroneutrality constraint enforces coupling between moving species (since, for example, the motion of one charged species through the membrane must now be offset by the countermotion of a second charged species so as to maintain local electroneutrality everywhere). This constraint magnifies the influence of minority carrier species and greatly restricts the possible transport scenarios available to a permeation experiment compared to a conduction experiment.

Although any model of multi-species ionic transport in perovskite systems could consider as many as four mobile species simultaneously (electrons, holes, protons, and oxygen ions/vacancies), in practice only three mobile defects at maximum will be important at any given time. This is due to the recombination of electrons and holes, which means that only one electronic species (either electrons or holes) will contribute to transport under a given condition. In oxidizing conditions, holes will be the dominant electronic defect species, while in reducing conditions electrons will be the dominant electronic defect species. This division enables the separation of multi-species permeation transport in perovskites into two tripolar transport cases: a case where protons, oxygen vacancies, and holes are present and a case where protons, oxygen vacancies, and electrons are present. Both cases have been formally treated previously by Virkar,[11] but will be reviewed here for completeness and to help build the foundation upon which our new model is constructed. Virkar's first case (protons, oxygen vacancies, and holes) is most relevant to the conditions of experimental interest examined in this paper, although both cases will be revisited later. Under the case of oxidizing conditions (p_{H_2O}, $p_{O_2} \gg p_{H_2}$), multi-species transport of protons, oxygen vacancies, and holes leads to the possibility that both water and oxygen can simultaneously permeate through a representative membrane, with the corresponding chemical flux expressions (j_{H_2O} and j_{O_2}) given by Virkar[11] as:

$$j_{H_2O} = -\frac{C_{OH_O^\bullet} B_{OH_O^\bullet} (C_{h^\bullet} B_{h^\bullet} + 4 C_{V_O^{\bullet\bullet}} B_{V_O^{\bullet\bullet}})}{4(C_{OH_O^\bullet} B_{OH_O^\bullet} + C_{h^\bullet} B_{h^\bullet} + 4 C_{V_O^{\bullet\bullet}} B_{V_O^{\bullet\bullet}})} \nabla \mu_{H_2O}$$
$$+ \frac{C_{OH_O^\bullet} B_{OH_O^\bullet} C_{h^\bullet} B_{h^\bullet}}{8(C_{OH_O^\bullet} B_{OH_O^\bullet} + C_{h^\bullet} B_{h^\bullet} + 4 C_{V_O^{\bullet\bullet}} B_{V_O^{\bullet\bullet}})} \nabla \mu_{O_2} \tag{1}$$

and

$$j_{O_2} = \frac{C_{OH_O^\bullet} B_{OH_O^\bullet} C_{h^\bullet} B_{h^\bullet}}{8(C_{OH_O^\bullet} B_{OH_O^\bullet} + C_{h^\bullet} B_{h^\bullet} + 4 C_{V_O^{\bullet\bullet}} B_{V_O^{\bullet\bullet}})} \nabla \mu_{H_2O}$$
$$- \frac{C_{h^\bullet} B_{h^\bullet} (C_{OH_O^\bullet} B_{OH_O^\bullet} + 4 C_{V_O^{\bullet\bullet}} B_{V_O^{\bullet\bullet}})}{16(C_{OH_O^\bullet} B_{OH_O^\bullet} + C_{h^\bullet} B_{h^\bullet} + 4 C_{V_O^{\bullet\bullet}} B_{V_O^{\bullet\bullet}})} \nabla \mu_{O_2} \tag{2}$$

where C_j is the concentration of defect species j, B_j is that defect's mobility, and μ_i is the chemical potential gradient of chemical species i. A critical assumption of Virkar's derivation is that the flux of pure hydrogen across the membrane under oxidizing conditions is zero ($j_{H_2} = 0$). In other words, any transport of protons across the membrane under oxidizing conditions will involve the production/consumption of H_2O rather than H_2 on the two sides of the membrane. This is a reasonable assumption given the thermodynamic equilibrium between H_2O, O_2, and H_2, which under oxidizing conditions strongly favors H_2O over H_2. The most important outcome of the above expressions is that the flux of each chemical species is dependent on the gradients of BOTH species. This constraint has important consequences, one of which is that under most operating conditions, knowledge of both the oxygen and water gradients across the membrane are needed to determine the overall transport behavior.

2.2 Permeation transport limiting cases

Under certain situations, the multi-species transport equations introduced above can be simplified. In particular, simplification is possible under three limiting cases when only two of the three possible defects contribute to transport ("bipolar" transport). The three limiting cases are: a first case where transport is dominated by protons and oxygen ions, a second case where transport is dominated by protons and holes; and a final limiting case where transport is dominated by oxygen ions and holes. In Appendix A, one of these simplifying cases is treated in detail under the assumption of oxidizing conditions (producing an analogous set of limiting cases under reducing conditions can be achieved with only minor differences). The principle results of this treatment are presented in Fig. 1.

As shown in Fig. 1(a), bipolar transport of protons and oxygen ions (Case Ia) is the fundamental basis of steam permeation. The chemical transport of steam may be described by the flux equation indicated on the diagram. As discussed in the appendix, this flux equation can be converted into a Fick's First Law type expression which takes the general form:

$$j_i = -\tilde{D}_i \frac{dC_i}{dx} \tag{3}$$

where j_i is the flux of chemical species i, $\tilde{D}_i$ is the effective chemical diffusivity of i, and dC_i/dx is the concentration gradient of i. This approach enables the extraction of an effective chemical diffusivity for steam transport across the membrane, $\tilde{D}_{H_2O}$, due to the bipolar diffusion of protons and oxygen vacancies. Those familiar with perovskites will undoubtedly recognize this expression for Case Ia as the effective chemical diffusivity of steam proposed by Kreuer,[8,12] along with his description of the equilibrium concentration of protons within the system, known as the Degree of Hydration.

Case Ib, the bipolar transport of protons and holes, is illustrated in Fig. 1(b). This case represents the fundamental basis for a hydrogen transport membrane, since only protons and holes are transported. Fick's First Law simplification of the flux equation for this situation enables the extraction of an effective chemical diffusivity for hydrogen, $\tilde{D}_{H_2}$, which depends on the diffusivity of both the protons and holes as well as the relative concentrations of protons *versus* holes. In analogy to the degree of hydration factor used for Case Ia, the relative concentration of protons *versus* holes may be described by a "degree of protonation" factor, X'. While Case Ib in essence represents a pure
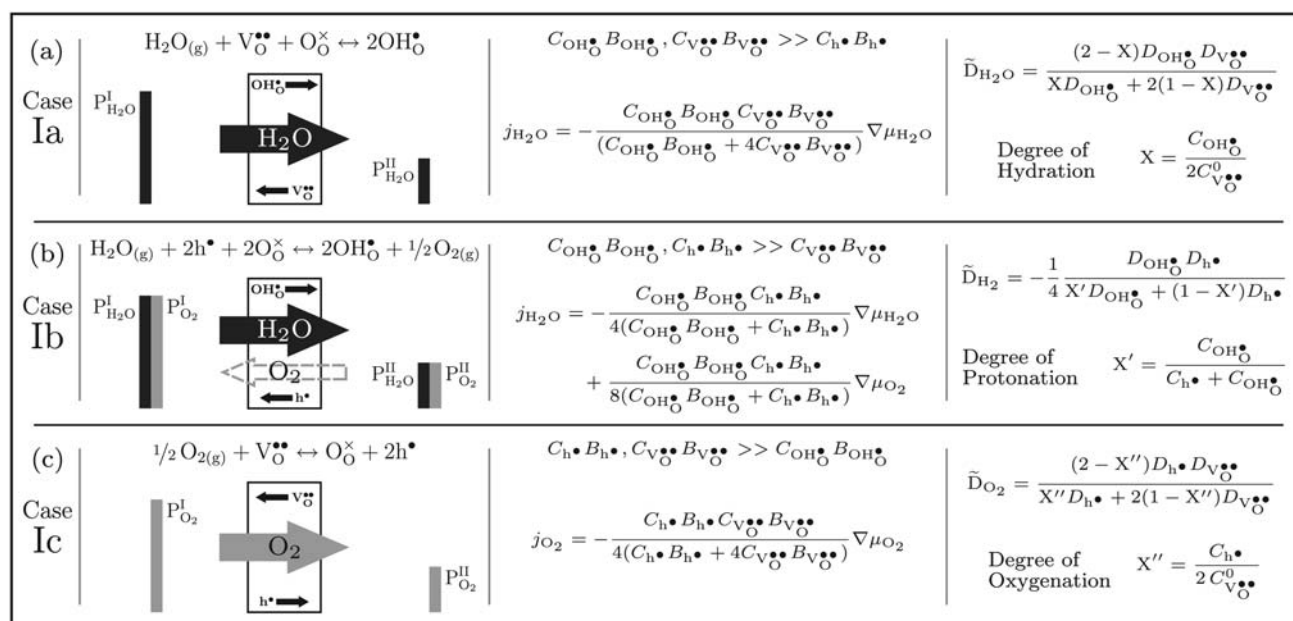
(a) Case Ia

$$H_2O_{(g)} + V_O^{\bullet\bullet} + O_O^\times \leftrightarrow 2OH_O^\bullet$$

$$C_{OH_O^\bullet} B_{OH_O^\bullet},\, C_{V_O^{\bullet\bullet}} B_{V_O^{\bullet\bullet}} \gg C_{h^\bullet} B_{h^\bullet}$$

$$j_{H_2O} = -\frac{C_{OH_O^\bullet} B_{OH_O^\bullet} C_{V_O^{\bullet\bullet}} B_{V_O^{\bullet\bullet}}}{(C_{OH_O^\bullet} B_{OH_O^\bullet} + 4 C_{V_O^{\bullet\bullet}} B_{V_O^{\bullet\bullet}})} \nabla \mu_{H_2O}$$

$$\tilde{D}_{H_2O} = \frac{(2 - X) D_{OH_O^\bullet} D_{V_O^{\bullet\bullet}}}{X D_{OH_O^\bullet} + 2(1 - X) D_{V_O^{\bullet\bullet}}}$$

Degree of Hydration $\quad X = \dfrac{C_{OH_O^\bullet}}{2 C_{V_O^{\bullet\bullet}}^0}$

(b) Case Ib

$$H_2O_{(g)} + 2h^\bullet + 2O_O^\times \leftrightarrow 2OH_O^\bullet + 1/2\,O_{2(g)}$$

$$C_{OH_O^\bullet} B_{OH_O^\bullet},\, C_{h^\bullet} B_{h^\bullet} \gg C_{V_O^{\bullet\bullet}} B_{V_O^{\bullet\bullet}}$$

$$j_{H_2O} = -\frac{C_{OH_O^\bullet} B_{OH_O^\bullet} C_{h^\bullet} B_{h^\bullet}}{4(C_{OH_O^\bullet} B_{OH_O^\bullet} + C_{h^\bullet} B_{h^\bullet})} \nabla \mu_{H_2O} + \frac{C_{OH_O^\bullet} B_{OH_O^\bullet} C_{h^\bullet} B_{h^\bullet}}{8(C_{OH_O^\bullet} B_{OH_O^\bullet} + C_{h^\bullet} B_{h^\bullet})} \nabla \mu_{O_2}$$

$$\tilde{D}_{H_2} = -\frac{1}{4}\frac{D_{OH_O^\bullet} D_{h^\bullet}}{X' D_{OH_O^\bullet} + (1 - X') D_{h^\bullet}}$$

Degree of Protonation $\quad X' = \dfrac{C_{OH_O^\bullet}}{C_{h^\bullet} + C_{OH_O^\bullet}}$

(c) Case Ic

$$1/2\,O_{2(g)} + V_O^{\bullet\bullet} \leftrightarrow O_O^\times + 2h^\bullet$$

$$C_{h^\bullet} B_{h^\bullet},\, C_{V_O^{\bullet\bullet}} B_{V_O^{\bullet\bullet}} \gg C_{OH_O^\bullet} B_{OH_O^\bullet}$$

$$j_{O_2} = -\frac{C_{h^\bullet} B_{h^\bullet} C_{V_O^{\bullet\bullet}} B_{V_O^{\bullet\bullet}}}{4(C_{h^\bullet} B_{h^\bullet} + 4 C_{V_O^{\bullet\bullet}} B_{V_O^{\bullet\bullet}})} \nabla \mu_{O_2}$$

$$\tilde{D}_{O_2} = \frac{(2 - X'') D_{h^\bullet} D_{V_O^{\bullet\bullet}}}{X'' D_{h^\bullet} + 2(1 - X'') D_{V_O^{\bullet\bullet}}}$$

Degree of Oxygenation $\quad X'' = \dfrac{C_{h^\bullet}}{2 C_{V_O^{\bullet\bullet}}^0}$

Fig. 1 Simplifications of full multi-species transport equations for the three bipolar limiting cases.

hydrogen transport membrane, under oxidizing conditions any protons crossing the membrane will immediately react with the oxygen present, resulting in the appearance of water (rather than molecular hydrogen) moving across the membrane. As is reflected in the defect reaction accompanying Fig. 1(b), this also causes an "apparent" flux of oxygen across the membrane in the opposite direction, since oxygen is consumed where steam is produced, and oxygen is produced where steam is consumed. Thus, under oxidizing conditions, Case Ib results in "apparent" fluxes of both oxygen and water moving in opposite directions across the membrane, with the apparent molar flux of oxygen exactly half that of the water flux.

Case Ic, the bipolar transport of oxygen vacancies and holes, is illustrated in Fig. 1(c). This situation is favored under extremely oxidizing and dry high-temperature conditions and represents the fundamental basis for an oxygen transport membrane. In analogy to the previous cases, Fick's First Law simplification of the flux equation for this situation enables the extraction of an effective chemical diffusivity for oxygen, $\tilde{D}_{O_2}$, that depends on the diffusivity of both the oxygen ions and holes as well as the relative concentrations of oxygen vacancies *versus* holes. In analogy to the degree of hydration and degree of protonation factors used previously, the relative concentration of oxygen vacancies *versus* holes may be described by a "degree of oxygenation" factor, X''.

It is important to note that for each limiting bipolar diffusion case discussed above, the effective chemical diffusivity depends on both defect species present, one of which is typically the majority transport carrier, and the second of which is typically the minority species. The overall effective chemical diffusivity measured during a permeation experiment therefore represents a blending of these two defect species in a way which accentuates the influence of the minority species. For instance, the chemical diffusivity of H_2O in the limit of full hydration (where protons are dominant and oxygen vacancies are rare), depends only on

the diffusivity of the oxygen vacancies. This is in direct contrast to the situation in a conductivity experiment, where the overall conductivity is determined by the summation of the individual partial conductivities of each mobile charged species.[13]

2.3 Multi-species transport space diagram

In a system consisting of three possible point defects, the full range of all possible tripolar transport scenarios, including each of the three two-species limiting cases discussed above, can be captured using a ternary transport diagram, as illustrated in Fig. 2. The basic idea for this ternary transport diagram representation was first presented by Bonanos in a European Science Foundation presentation in 2007.[6] Bonanos introduced this diagram in the context of mixed-conducting fuel cells; however, in the discussion that follows, we will significantly expand this representation and use it to explore the differences between conduction and permeation in these multi-species systems.
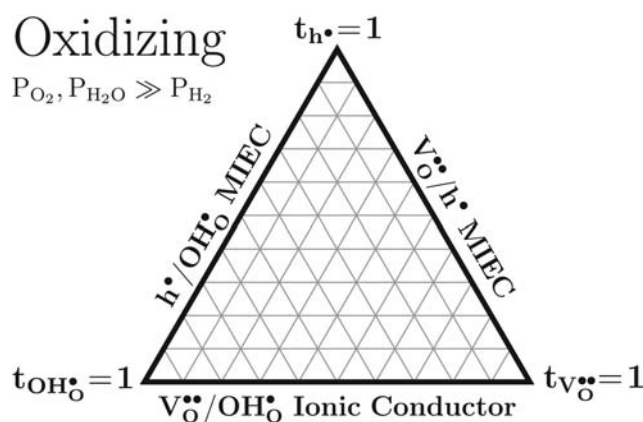

Fig. 2 Schematic of a graphical representation of all possible multi-species transport possibilities in oxidizing conditions.

The ternary transport diagram illustrated in Fig. 2 presents the full range of multi-species transport scenarios which are possible in a tri-species proton, oxygen ion, and hole conductor. This diagram is applicable to the typical protonic perovskite system under oxidizing conditions, where protons, oxygen ions, and holes are the three major mobile defect species. The diagram delineates all possible combinations of transference number for each of the three mobile species. Examining Fig. 2 in this context, the three vertices of the triangle represent the limiting cases where only a single species (either protons, oxygen ions, or holes) contributes to transport, while the edges of the triangle represent the range of possible two-species transport scenarios, and the interior of the triangle represents the range of possible three-species transport scenarios.

Conduction imposes no fundamental constraints on multi-species transport, and therefore in a conduction process, any region of this ternary transport diagram is theoretically accessible. This is not true for permeation, however. The additional internal electroneutrality constraint imposed by permeative transport means that only certain multi-species transport combinations are permitted in order to maintain charge balance.

The specific combinations of multi-species transport that are permitted in a permeation process can be described by one of three sets of linear equations. The first equation in all sets is associated with the definition of transference number

$$t_{OH_O^\bullet} + t_{h^\bullet} + t_{V_O^{\bullet\bullet}} = 1 \tag{4}$$

while a second equation is necessary to impart the electroneutrality restriction and is dependent on the direction of the three defect species. Electroneutrality relationships, written in terms of fluxes

$$j_{OH_O^\bullet} - j_{h^\bullet} - 2j_{V_O^{\bullet\bullet}} = 0 \tag{5}$$

$$-j_{OH_O^\bullet} + j_{h^\bullet} - 2j_{V_O^{\bullet\bullet}} = 0 \tag{6}$$

$$-j_{OH_O^\bullet} - j_{h^\bullet} + 2j_{V_O^{\bullet\bullet}} = 0 \tag{7}$$

impart the necessary directionality (taking left to right as positive) and charge sign (there are six actual permutations, however, the other three are degenerate inverses of eqn (5)–(7)). For simplicity, an alternate, but equivalent, definition for transference numbers based on fluxes rather than conductivities is used in this approach that accounts for issues associated with directionality.

$$t_j = \frac{|z_j j_j|}{\sum |z_j j_j|} \tag{8}$$

where t_j is the transference number for defect species j, z_j is the charge of defect species j, and j_j is the molar flux of defect species j. The absolute values of the quantities must be used in order to make the definition consistent with the traditional definition of transference numbers which lack indications of charge type and directionality. Replacing the fluxes in eqn (5)–(7) with transference numbers produces the following independent electroneutrality relationships

$$t_{OH_O^\bullet} - t_{h^\bullet} - t_{V_O^{\bullet\bullet}} = 0 \tag{9}$$

$$-t_{OH_O^\bullet} + t_{h^\bullet} - t_{V_O^{\bullet\bullet}} = 0 \tag{10}$$

$$-t_{OH_O^\bullet} - t_{h^\bullet} + t_{V_O^{\bullet\bullet}} = 0 \tag{11}$$

These allowable combinations manifest on the diagram as a set of three "tie-lines" which bisect the ternary diagram as shown in Fig. 3(a).

The tie-lines shown in Fig. 3(a) terminate on the edges of the diagram at three distinct points. These three points represent the three limiting binary-species (bipolar) permeation cases (Cases Ia, Ib, and Ic) previously delineated. Thus, point "a" on the diagram represents the limiting case of bipolar proton and oxygen ion permeation. As we have previously discussed, this limiting case is associated with pure steam transport across the membrane, as governed by the indicated equation on the diagram. Point "b" on the diagram represents the limiting case of bipolar proton and hole permeation, which leads to pure hydrogen transport across the membrane (although as we have previously discussed, in an oxidizing environment this instead leads to an apparent flux of H_2O in one direction across the membrane and an apparent flux of O_2 in the opposite direction that is half as large). Finally, point "c" on the diagram represents the limiting case of bipolar oxygen ion and hole permeation, which leads to pure oxygen transport across the membrane.

The three tie-lines connecting these three limiting cases delineate the possible tri-polar permeation processes which also satisfy internal charge balance. The permeation behavior along a particular tie-line can be interpreted as a "blending" of the behavior of the two limiting cases that bound that tie-line. Thus, for example, along the tie-line connecting points "a" and "b", H_2O and O_2 transport across the membrane in opposite directions, but in moving from "b" to "a," the relative amount of O_2 compared to H_2O crossing the membrane decreases continuously until at point "a" only H_2O crosses the membrane. Along the tie-line between points "a" and "c," O_2 again begins to transport across the membrane, but now in the same direction as H_2O. Moving from "a" towards "c," the relative amount of O_2 compared to H_2O crossing the membrane continuously increases until at point "c" only O_2 crosses the membrane. The third tie-line requires one of the two terminating reactions ("b" or "c") to operate in the reverse direction. This can therefore be described as the "b-c" tie-line. Moving from point "b" towards "c," the water transport in the positive direction slowly diminishes while the "apparent" counter-flux of oxygen is slowly replaced by a real flux of oxygen until at point "c" only O_2 crosses the membrane. A "blending ratio" can be used to describe the contributions of the two limiting cases to the overall flux. The "lever rule" used in phase diagrams can be used to find this ratio, R.

It should be noted that the entire tri-species transport diagram provided by Fig. 2 and 3(a) reflects the transport situation under oxidizing conditions only, when protons, oxygen vacancies, and holes are the three major transport species defects. A mirrored triangle can therefore be added to this transport space which reflects the situation under reducing conditions (i.e, in the

6274 | J. Mater. Chem., 2010, 20, 6271–6281

This journal is © The Royal Society of Chemistry 2010
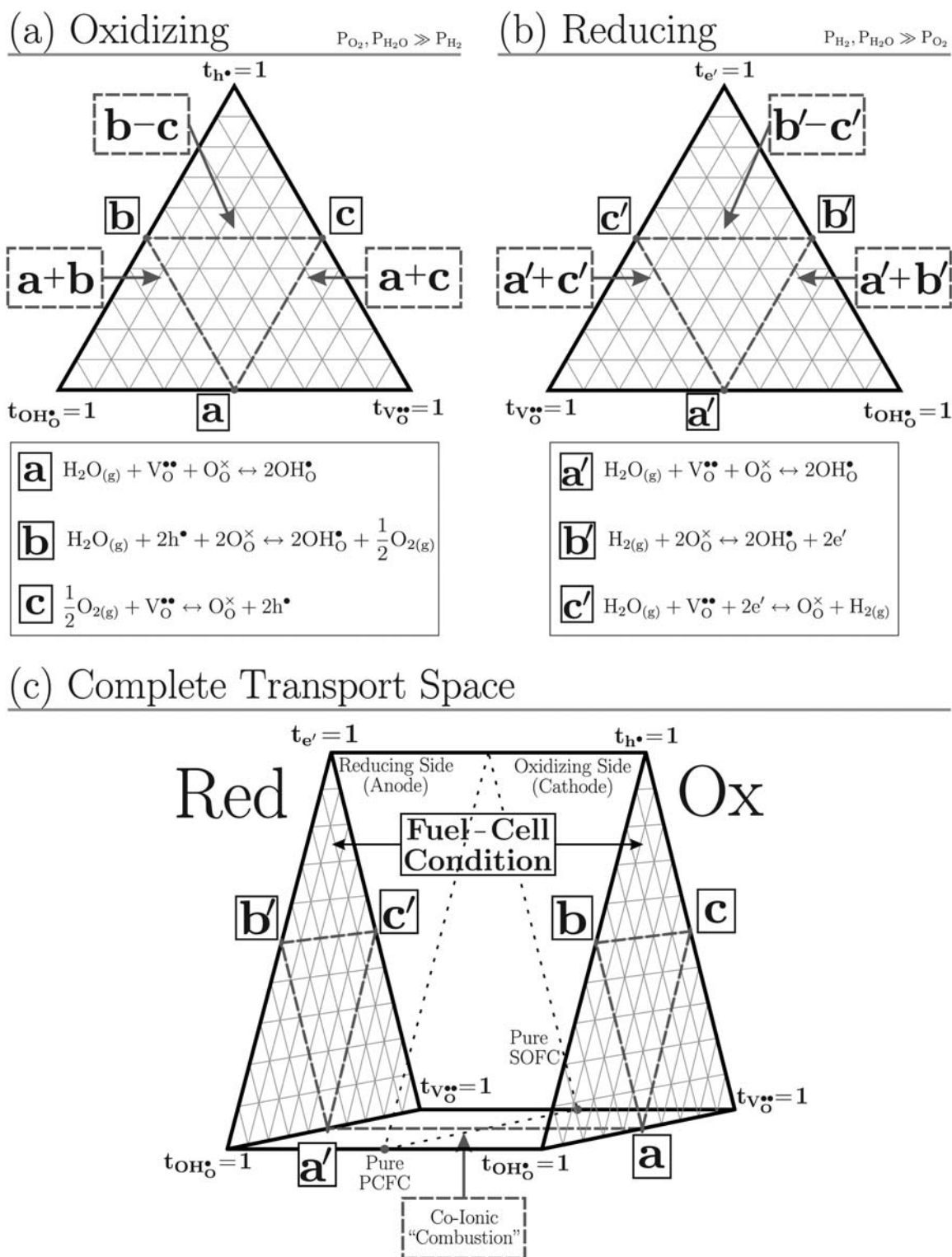
Fig. 3 Schematics of a graphical representation of the permeation possibilities within the Multi-Species Transport Space. The red dots correspond to the three two-species simplifications. All other three species permeation must occur along the three tie-lines between these points. (a) represents the transport under oxidizing conditions and (b) represents reducing conditions. (c) gives the relationship between the two conditions and represents the full transport space.

presence of hydrogen gas), where protons, oxygen vacancies, and electrons form the three major transport species defects. This situation is shown in Fig. 3(b). In this case, the electron hole vertex is replaced by an electron vertex.

The oxidizing conditions diagram provided in Fig. 3(a) and the reducing conditions diagram provided in Fig. 3(b) can be joined together to create a comprehensive diagram which summarizes the various conduction and permeation processes

available under all conditions. In order to link these two diagrams, it is necessary to add another region bridging the two transport triangles which captures scenarios where one side of the membrane is exposed to oxidizing conditions while the other side of the membrane is exposed to reducing conditions. We term this region the "Fuel Cell Region," as it reflects the conditions which are present in a fuel cell (one side oxidizing, one side reducing). The resulting comprehensive diagram, shown in Fig. 3(c) thus captures the complete transport space, including the three-dimensional region of combined oxidizing/reducing conditions.

We will focus brief attention on the two-dimensional co-ionic (proton/oxygen ion) "side" of this composite diagram. Several interesting features are apparent. First, as illustrated in the diagram, the classical protonic ceramic fuel cell (PCFC) is obtained when a pure proton conductor (which would lay on the $t_{OH_O^\bullet} = 1$ vertex/edge) is subjected to fuel cell conditions. At the other extreme, the classical solid-oxide fuel cell (SOFC) is obtained when a pure oxygen ion conductor (the $t_{V_O^{\bullet\bullet}} = 1$ vertex/edge) is employed. Under "fuel cell conditions," the only possibility for *permeative* transport involving only protons and oxygen ions (no electronic defects) is the pure co-ionic conduction of protons and oxygen ions. In this case, the protons are transported from the reducing (hydrogen rich) side of the membrane to the oxidizing (oxygen rich) side of the membrane, where they react with oxygen to produce water and oxygen ions. Oxygen ions are simultaneously transported from the oxidizing side of the membrane to the reducing side of the membrane, where they react with hydrogen to produce water and protons. The net effect is thus the effective combustion of hydrogen and oxygen to produce water on both sides of the membrane, mediated by the co-ionic transport of protons and oxygen ions in opposite directions. We term this process "co-ionic combustion." Importantly, perfect co-ionic permeation of protons and oxygen ions would be unsuitable for fuel cell applications, leading to an open circuit voltage (OCV) of zero due to the effective internal shorting due to the equal and opposite charge flow of protons and oxygen ions across the membrane (despite the fact that this material would still be a perfect electronic insulator!). In fact, any electrolyte material exhibiting a mixture of both proton and oxygen ion transport will suffer from a reduction in OCV. The OCV for a fuel cell made from a co-ionic conducting material would decrease from the theoretical Nernst voltage at the limit to zero at the co-ionic permeation limit ($t_{OH_O^\bullet} = 0.5$) before increasing again back to the full Nernst voltage at the $t_{V_O^{\bullet\bullet}} = 1$ limit. Thus, a material which is substantially an oxygen ion conductor but has a small amount of proton conductivity will still function as a fuel cell electrolyte but will necessarily show a reduction in OCV. The expected reduction in OCV can be calculated using the lever rule, given knowledge about the location of the candidate material along the co-ionic edge of the transport diagram. Similar analyses may be applied to the "oxygen transport" (mixed oxygen-ion/electronic defect) and "hydrogen transport" (mixed proton/electronic defect) sides of the diagram, taking into account electron-hole recombination. Analyses of the full four-species "interior" region of this three-dimensional diagram are also possible, but are beyond the scope of this paper.

3 Experimental

3.1 Test-bed design

In order to experimentally explore and verify the transport theories described in the previous section, an experimental test-bed was designed to study both steady state and transient transport of water and isotopically labeled water species through a tubular permeation membrane. A schematic of the setup is shown in Fig. 4. The $H_2O/D_2O/H_2^{18}O$ is introduced to the "wet" side of the membrane by flowing ultra-high purity (UHP) carrier gasses or air through temperature-controlled, insulated stainless steel bubblers and monitored using a humidity/dew point sensor (Omega CNITH-I8DH43-5-C4EI). UHP gas is dried with a water-trap (Agilent Glass Indicating Moisture Trap GMT4HP) for use on the "dry" side of the membrane. The exit composition is recorded with an atmospheric sampling mass spectrometer (MKS Cirrus™ Benchtop Atmospheric RGA System). Multi-gas, multi-composition calibrations are performed using MKS-provided software specifically for multi-point calibrations and the corrections are made automatically during data collection. The flow rates of both carrier gases are controlled with rotameters (Cole-Parmer 150-mm Correlated Flowmeters with High-Resolution Valves). All gas and sampling lines are heated using heater rope (Omegalux®FGR Series) with a 120V variable voltage controller and insulated with flexible woven silica fabric. Line temperatures are kept above 60 °C to avoid condensation; the temperature can be increased for higher water partial pressures, up to at least 110 °C. The isotope water bubbler is filled with one of a variety of isotope mixtures, either D_2O (99.9% purity), 9 parts D_2O (99.9% purity) and 1 part $H_2^{18}O$ (10% purity), 1 part H_2O and 1 part $H_2^{18}O$ (10% purity), or $H_2^{18}O$ (99.9% purity). The use of different carrier gases for each side of the membrane allows for additional monitoring of leaks in the high-temperature seals.

Measurements from the mass spectrometer are made as absolute pressures (P_i torr). Some simple operations are necessary to convert this data into a more usable form, either partial pressures (p_i torr/torr) or, more importantly, molar flow rates (n_i mol/s). To determine partial pressure, the absolute measurement for each mass is divided by a sum of all the absolute
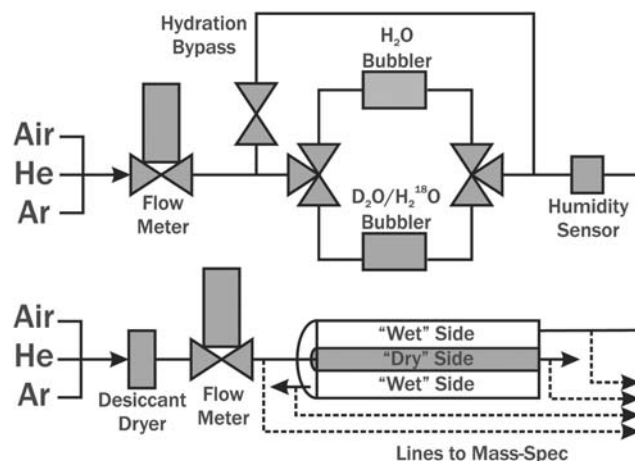

Fig. 4 A schematic of the steam permeation measurement test-bed.

measurements for that sweep. These partial pressures are then multiplied by the molar flow rate of the carrier gas to produce molar flow rates for the individual masses. For permeating species, division by the active surface area of the membrane enables further conversion to the more general molar flux (j_i mol/cm^2 s).‡

3.2 Membrane tube production

For these permeation experiments, yttrium-doped barium zirconate (BaZr$_{0.8}$Y$_{0.2}$O$_3$ or BZY20) was chosen, based on its good ionic conductivity and high chemical stability in water environments,[8] which for these experiments, sometimes days in duration, is extremely important. BZY20 tubes were extruded as raw components and sintered using the SSRS process.[14] 0.4% NiO by weight was added, which is approximately 1.5 mole percent. The tubes reached a final density of 99% of the theoretical density with grain sizes of 1–4μm. The final diameter was 6mm with a wall thickness of 1mm. The high density and large grain size obtained for these tubes was an important and highly desirable outcome, as it helps to reduce unwanted influences on the transport behavior from porosity and/or grain boundaries.

4 Results and discussion

One of the most important predictions of multi-species transport theory in perovskite materials is that steam permeation should be observed under oxidizing conditions except for membranes operated at point "c" in the transport space diagram. Despite the fact that steam permeation should be a widespread feature of these materials, however, the phenomenon has rarely been explicitly explored either theoretically or experimentally. Besides the pioneering theoretical work of Kreuer and Maier,[12,15] few have developed theory directly concerning multi-species diffusion leading to the chemical permeation of steam in perovskites[11,16] and only a handful of experimental explorations have taken steam permeation into account.[7,17,18] Recent work by Han-Ill Yoo and colleagues[9,10] has implicated multi-species transport to explain the unusual hydration and conduction dynamics observed in these materials upon exposure to step changes in water or oxygen, although these contributions did not consider steady-state steam permeation.

4.1 Isotope exchange experiment

While there is some prior experimental evidence substantiating the phenomenon of steam permeation in barium cerate ceramics,[18] the phenomenon has never been experimentally quantified in barium zirconate ceramics. Furthermore, these earlier experiments subjected one side of the permeation membrane to vacuum conditions, reflecting an unrealistic operating condition and making quantification difficult. Therefore in this study an atmospheric isotope exchange permeation experiment was developed in order to demonstrate steam permeation in barium zirconate under realistic conditions. In this experiment, a BZY20 permeation membrane tube was first allowed to

---

‡ In many cases, overlapping mass signals required careful data deconvolution before mass balance analyses could be completed. The details of this deconvolution process are described in Appendix B.
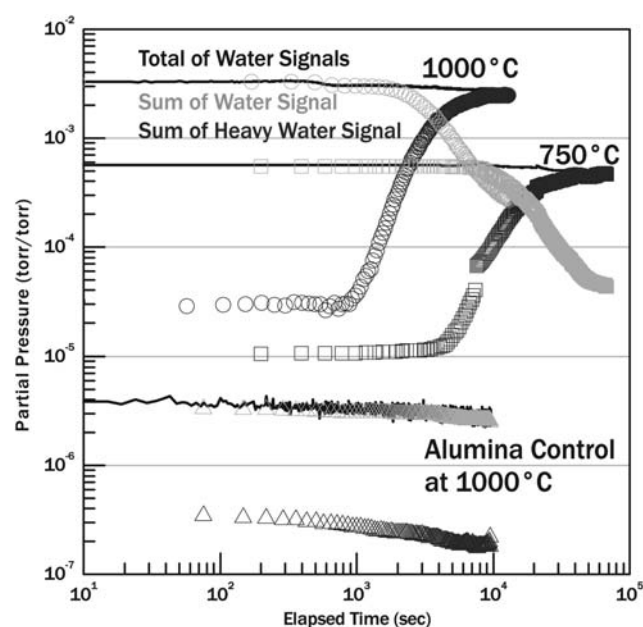
Fig. 5 D$_2$O Exchange of Steam Permeable Membrane at 1000 °C and 750 °C. The H$_2$O to D$_2$O switch was made at t = 0. The gray curves represent those signals attributable to water for each experiment, the blue to those attributable to heavy water. The lower set of lines is the measured signals from the 1000 °C alumina tube control experiment.

equilibrate with a H$_2$O/Ar mixture on the "wet" (feed) side of the membrane and dry Ar on the "dry" (permeate) side of the membrane. Then, at a specific time (t = 0), the H$_2$O on the feed side of the membrane was switched to D$_2$O and the mass spectrometer was used to monitor the time-resolved appearance of the isotopically labeled deuterated species as they gradually permeated across the BZY membrane. Fig. 5 graphically shows the resulting slow replacement of hydrogen by deuterium as the membrane, which was initially filled with permeating steam, incorporated the newly introduced D$_2$O. Due to the relatively slow rate at which isotope species appeared on the "dry" side compared to the rapid speed in which the water was exchanged out of the system on the "wet" side, this response was ascribed to true solid state steam permeation rather than leakage. In contrast, a control experiment using an alumina tube as a substitute for the BZY20 tube showed only a weak water signal. Alumina is not thought to be permeable by water, so any D$_2$O signal present on the permeate side of the alumina tube could be attributed to steam leaking through the glass seals. Even at 1000 °C, the heavy water signal was at or below the detection limit of the mass spectrometer, confirming active permeation through the BZY20 as the source of the elevated water signals and that leakage was not a significant contributor to the flux measurements.

The above interpretation of the isotope exchange experiment as steam-permeation requires the assumption that some or all of the water generated is due to bipolar diffusion of protons and oxygen ions. It is also possible to deduce that only protons are moving across the membrane (counterbalanced by holes), which then combine with available oxygen on the "dry" side of the membrane to generate the water signal measured. Experiments of the type above are unable to unequivocally determine which

mechanism, or mechanisms, is operating. Isotopically labeled oxygen time-lag experiments can provide the necessary evidence, however due to problems with the time-lag of measuring significant ^{18}O ions moving through an oxide *in situ*, such tests prove challenging to interpret. Therefore an additional experimental technique based on global system mass-balance was developed to provide the necessary evidence.

4.2 Mass balance studies

As just discussed, the simple isotope exchange experiment described above provided evidence for steam permeation but did not permit full quantification of the mechanism (or mechanisms) involved, and in particular did not permit quantification of the simultaneous permeation of oxygen, which is also predicted in these systems under most oxidizing conditions except at point "a" in the transport space diagram. In order to track both steam and oxygen permeation fluxes simultaneously and thus establish the full nature of the permeation mechanism, careful steady-state mass-balance studies were therefore performed on the permeation system under a variety of operating conditions. These mass-balance studies were achieved by simultaneous monitoring of the four inlets and outlets of the system under steady-state permeation conditions with the signals of all masses of interest being recorded. This process provided detailed bookkeeping of all the species and their evolution after passing across (or through) the active area of the permeation membrane.

The information provided by these mass balance studies enabled direct mapping of the permeation system behavior onto a specific point of the transport space diagram for each set of operating conditions measured, using nothing more than the experimentally measured permeation fluxes for water and oxygen. This provided an opportunity to directly relate experimentally observed permeation transport behavior to multi-species transport theory. The relevant data could eventually be distilled into a simple graphical format which visually summarizes the transport/exchange of the pertinent chemical species during steady state permeation at a given set of operating conditions.

Three representative experiments will be detailed here. For the first experiment, the analysis will be explained in more detail, with the other experiments following the same methods.

4.2.1 Experiment (a): 1000 °C—Helium with $H_2{}^{18}O$/Argon.
In this first mass-balance experiment, $H_2{}^{18}O$ steam (with helium as the carrier gas) was introduced into the feed side of a tubular BZY20 permeation membrane operating at 1000 °C. The permeate side of the membrane was provisioned with a dry (desiccated) argon carrier sweep gas.

Fig. 6(a) illustrates the results of the steady state mass-balance analysis for this experiment. The flux measurements for water and oxygen (0.493 and −0.12 mol/cm² s respectively) are direct evidence that steam-permeation is in fact occurring, and mostly by a co-ionic proton/oxygen vacancy mechanism, since the amount of oxygen that is consumed cannot remotely account for all of the water flux that is observed. Both protons and vacancies must therefore be transporting across the membrane in addition to a small contribution from holes. It is possible to calculate the transference numbers of all three defect species from the

measured permeation fluxes of H_2O and O_2, since the relationship between the various species is constrained such that the system must lie on one of the tie-lines and must also produce the measured permeating chemical fluxes (j_{H_2O} and j_{O_2}). By employing the following set of equations, the defect fluxes, complete with direction, may be calculated from the measured chemical permeation fluxes of H_2O and O_2

$$j_{OH_O^\bullet} = 2j_{H_2O} \tag{12}$$

$$j_{h^\bullet} = 4j_{O_2} \tag{13}$$

$$j_{V_O^{\bullet\bullet}} = -\left(j_{H_2O} + 2j_{O_2}\right) \tag{14}$$

These defect fluxes can then be used to calculate the transference numbers and thereby specify the operating point of the system in the transport space diagram. Once the transference numbers have been found, the "blending ratio," R, can also be determined, enabling the system's overall transport behavior to be interpreted in terms of a mixture of the bounding bipolar transport mechanisms. It is also possible to quickly ascertain which tie-line a given permeation experiment falls on using simple inspection. If the steam and oxygen fluxes are in opposite directions and the steam to oxygen ratio is greater than 2, the system must be operating on the "a + b" tie-line, while for ratios smaller than 2, the system is operating on the "b − c" tie line. Finally, if the steam and oxygen fluxes are in the same direction, then the system must be operating somewhere on the "a + c" tie-line.

An important result from the mass balance experiment in Fig. 6(a) is the evidence of oxygen generation on the "wet" side and oxygen consumption on the "dry" side of the membrane. Although the oxygen flux is small, this is direct evidence that under the operating conditions of this experiment, holes are also participating in transport, and that permeation is occurring along the "a + b" tie-line. In fact, using the technique discussed above we are able to specify precisely where this experiment is operating on the transport space diagram. As shown in Fig. 6(a), in this experiment steam permeation is attributable to both the bipolar proton/oxygen ion diffusion (mechanism "a") as well as the bipolar proton/hole diffusion (mechanism "b"), although the bulk ($\sim$ 95%) of the steam permeation is due to mechanism "a". Thus, the operating conditions in this particular experiment lead to permeation behavior close to the co-ionic (bipolar proton/oxygen-ion) limit, and holes have only a very minor, although still measurable, effect on transport.

4.2.2 Experiment (b): 750 °C—Helium with 5% $H_2{}^{18}O$/Argon.
In this second experiment, 5% $H_2{}^{18}O$ steam (with helium as the carrier gas) was introduced into the feed side of a tubular BZY20 permeation membrane operating at 750 °C. The permeate side of the membrane was again provisioned with a dry (desiccated) argon carrier sweep gas.

The results are summarized in Fig. 6(b). Unlike the situation in Experiment (a), in this experiment the holes contribute more than the vacancies to the overall transport balance. The decreased operating temperature in this experiment significantly reduces both the concentration and mobility of oxygen
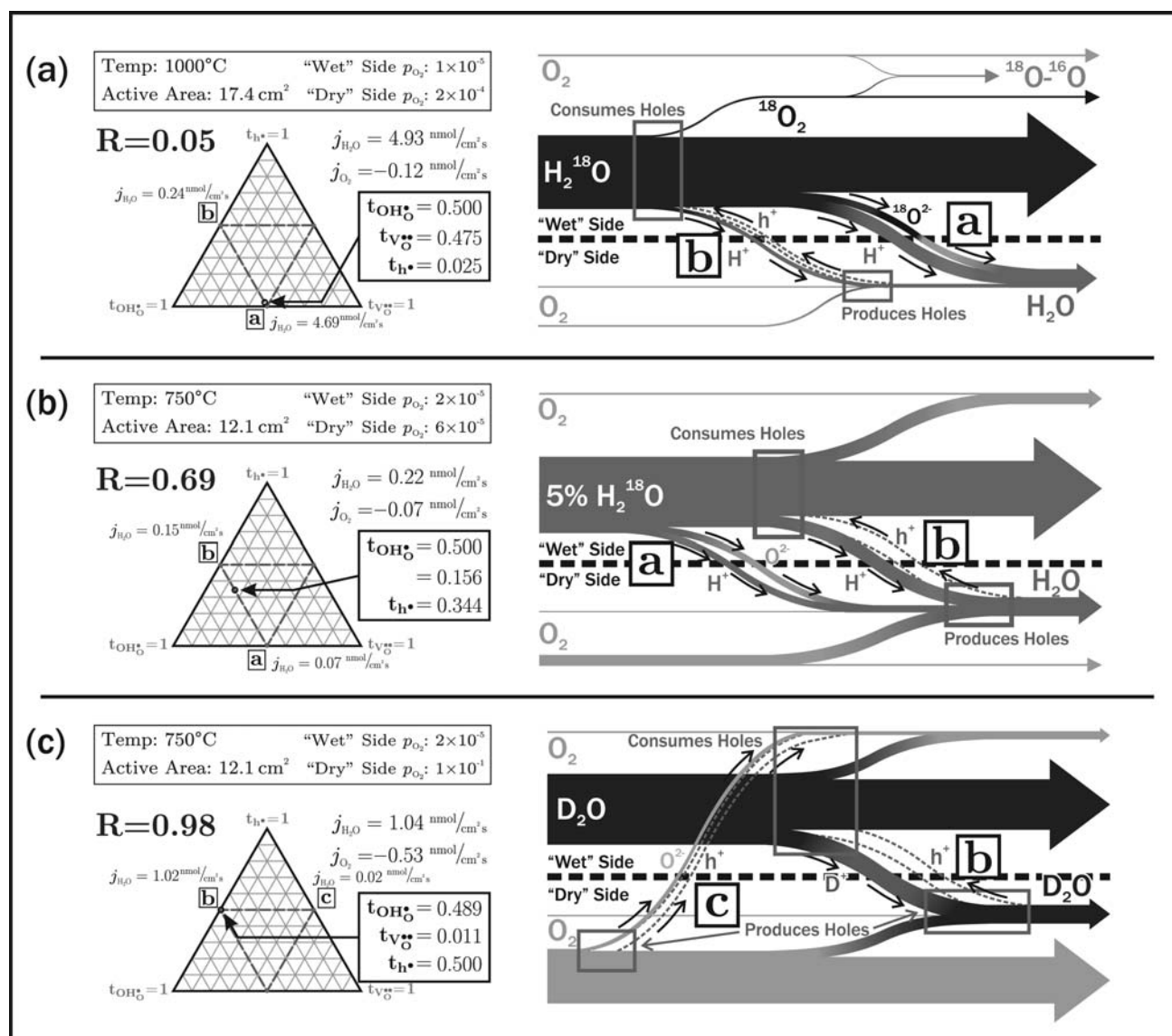
Fig. 6 Illustration of the mass balance results for all three reported experiments.

vacancies, thereby favoring the participation of holes. This increase in hole participation is a clear indication that permeation operates farther up the "a + b" tie-line under these experimental conditions, as confirmed by Fig. 6(b) (exact location established using the same procedure described previously for Experiment (a)). With approximately a 30%/70% split between mechanism "a" and mechanism "b" transport, a description of permeation behavior in this system clearly involves both Case Ia and Case Ib bipolar transport models.

4.2.3 Experiment (c): 750 °C—Argon with D$_2$O/Air. In Experiment (c) the effect of higher permeate-side oxygen partial pressures on the flux and the position within the transport space was explored. Still at 750 °C, D$_2$O saturated argon gas was used this time on the "wet" (feed) side while dry (desiccated) air was fed to permeate side of the membrane.

The results are summarized in Fig. 6(c). The higher oxygen pressure further increases the role of holes, and so under these

conditions it is observed that holes and protons participate almost exclusively in transport, while oxygen vacancies have a very limited role. Additionally, the complementary driving force due to the large oxygen partial pressure gradient across the membrane and the high mobility of holes as compared to oxygen vacancies has led to a five-fold increase in steam flux, as compared to Experiment (b). As shown in Fig. 6(c), this experiment is determined to be operating close to position "b" on the transport space diagram, although slightly onto the "b − c" tie line, corresponding to nearly pure bipolar proton/hole permeation with a very slight contribution from oxygen vacancies. This is also the first evidence that permeation behavior associated with the "b − c" tie-line is achievable under typical experimental conditions.

The experimental conditions explored here are merely a small sliver of the possible combinations achievable using the permeation test-bed. Testing is on-going, with the future intent of achieving permeation conditions along the "a + c" tie-line and
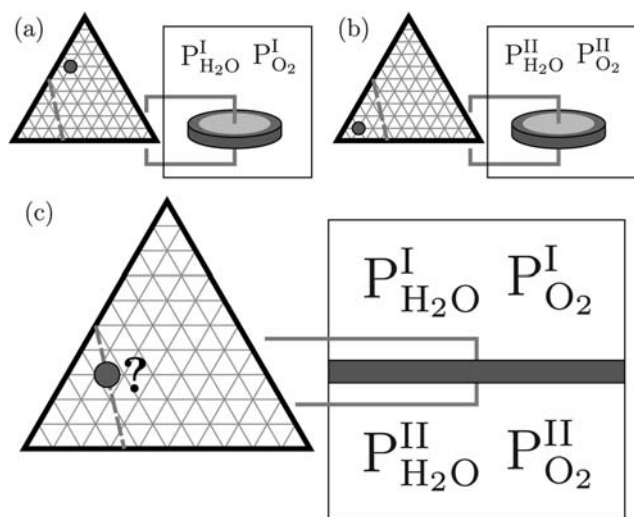
Fig. 7 Although the feasibility is not yet known, it may be possible to take conductivity measurements at two different atmospheres (a) and (b), and predict the resulting permeation behavior, (c), of a permeation membrane separating the two environments.

the mapping of entire tie-lines. These efforts should enable the ability to predict permeation results based on the experimental conditions.

4.3 Unification of conductivity and permeation

A larger question remains; is there a relationship between measurements of conductivity and permeation? Or to be more precise, is there a way to predict the location of a permeation experiment on the transport space diagram based on simple conductivity measurements? One of the ultimate goals of the transport space theory is to take the results of conductivity measurements at two different atmospheres, as shown in Fig. 7 (a) and (b), and determine the permeation system behavior that would result if those two atmospheres were imposed on opposite sides of a permeation membrane, seen as (c).

5 Conclusions

For perovskites, such as BZY20, multi-species transport is a significant factor and it is therefore critical to understand the role that minority defects may play under a wide variety of possible conditions. The transport space theory presented in this paper will help researchers make determinations about the conditions that may result in significant contributions from minority carrier species and/or require the use of multi-species modeling approaches. Such information may prove invaluable when trying to make determinations of the majority carrier defect or the source of parasitic OCV losses when considering these materials for fuel cell electrolytes or other electrochemical applications.

Permeation experiments using isotope tracing are an interesting and vital tool to investigate multi-species transport because they accentuate the role of minority species while still providing a way to track the majority species. The results from these experiments can be directly translated onto the transport space diagram, producing an avenue for intuitive interpretation

of transport behavior and a direct determination of transference numbers.

Appendix A

The process used below to find the transport equations for the hole/proton limiting case is similar to that for the other two cases. The hole/proton case was selected for a detailed derivation since, unlike the well known proton/vacancy case, it is not found elsewhere in the literature.

Because oxygen vacancy diffusivity is often orders of magnitude lower than both proton and hole diffusivity, transport will frequently be dominated by protons and holes rather than protons and oxygen vacancies. Under oxidizing conditions, this scenario results in the transport of H_2O across the membrane in one direction and the "apparent" transport of O_2 across the membrane in opposite direction. Fig. 1(b) shows this case schematically, along with the relevant reaction. For this case, $C_{OH_O^\bullet} B_{OH_O^\bullet}, C_{h^\bullet} B_{h^\bullet} \gg C_{V_O^{\bullet\bullet}} B_{V_O^{\bullet\bullet}}$ which simplifies the flux relationship previously given in eqn (1) to

$$j_{H_2O} = -\frac{C_{OH_O^\bullet} B_{OH_O^\bullet} C_{h^\bullet} B_{h^\bullet}}{4\left(C_{OH_O^\bullet} B_{OH_O^\bullet} + C_{h^\bullet} B_{h^\bullet}\right)} \nabla \mu_{H_2O}$$
$$+ \frac{C_{OH_O^\bullet} B_{OH_O^\bullet} C_{h^\bullet} B_{h^\bullet}}{8\left(C_{OH_O^\bullet} B_{OH_O^\bullet} + C_{h^\bullet} B_{h^\bullet}\right)} \nabla \mu_{O_2} \tag{A.1}$$

Factoring out the coefficients leads to

$$j_{H_2O} = \frac{C_{OH_O^\bullet} B_{OH_O^\bullet} C_{h^\bullet} B_{h^\bullet}}{\left(C_{OH_O^\bullet} B_{OH_O^\bullet} + C_{h^\bullet} B_{h^\bullet}\right)}\left(-\frac{1}{4}\nabla \mu_{H_2O} + \frac{1}{8}\nabla \mu_{O_2}\right) \tag{A.2}$$

It is now possible to find a relationship for two chemical gradients with respect to the two defect species,

$$2\nabla \mu_{OH_O^\bullet} + \frac{1}{2}\nabla \mu_{O_2} = \nabla \mu_{H_2O} + 2\nabla \mu_{h^\bullet}$$
$$-\frac{1}{4}\nabla \mu_{H_2O} + \frac{1}{8}\nabla \mu_{O_2} = \frac{1}{2}\nabla \mu_{h^\bullet} - \frac{1}{2}\nabla \mu_{OH_O^\bullet} \tag{A.3}$$

The chemical potential gradient of the lattice oxygen has been ignored, based on the low concentration of oxygen lattice defects compared to the oxygen lattice. Assuming ideal dilute defect concentrations, concentration gradients can be derived from the chemical potential gradients using

$$\nabla \mu_i = \frac{\partial \ln a_i}{\partial \ln C_i}\frac{RT}{C_i}\nabla C_i = \frac{RT}{C_i}\nabla C_i \tag{A.4}$$

Which leads to

$$\frac{1}{2}\nabla \mu_{h^\bullet} - \frac{1}{2}\nabla \mu_{OH_O^\bullet} = \frac{RT}{2}\left[\frac{\nabla C_{h^\bullet}}{C_{h^\bullet}} - \frac{\nabla C_{OH_O^\bullet}}{C_{OH_O^\bullet}}\right] \tag{A.5}$$

Substituting back into eqn (A.2),

$$j_{H_2O} = \frac{C_{OH_O^\bullet} B_{OH_O^\bullet} C_{h^\bullet} B_{h^\bullet}}{\left(C_{OH_O^\bullet} B_{OH_O^\bullet} + C_{h^\bullet} B_{h^\bullet}\right)}\left[\frac{RT}{2}\left(\frac{\nabla C_{h^\bullet}}{C_{h^\bullet}} - \frac{\nabla C_{OH_O^\bullet}}{C_{OH_O^\bullet}}\right)\right] \tag{A.6}$$

Converting mobilities into diffusivities using the Nernst-Einstein relationship, the equation becomes

$$j_{H_2O} = \frac{C_{OH_O^\bullet} D_{OH_O^\bullet} C_{h^\bullet} D_{h^\bullet}}{2\left(C_{OH_O^\bullet} D_{OH_O^\bullet} + C_{h^\bullet} D_{h^\bullet}\right)}\left(\frac{\nabla C_{h^\bullet}}{C_{h^\bullet}} - \frac{\nabla C_{OH_O^\bullet}}{C_{OH_O^\bullet}}\right) \quad (A.7)$$

Assuming that since there is no concentration gradient for oxygen vacancies and charge electroneutrality must be locally maintained, then $\nabla C_{h^\bullet} = -\nabla C_{OH_O^\bullet}$, and the relation can be further simplified to

$$j_{H_2O} = -\frac{D_{OH_O^\bullet} D_{h^\bullet}\left(C_{OH_O^\bullet} + C_{h^\bullet}\right)}{2\left(C_{OH_O^\bullet} D_{OH_O^\bullet} + C_{h^\bullet} D_{h^\bullet}\right)}\nabla C_{OH_O^\bullet} \quad (A.8)$$

At this point, it is helpful to introduce a new quantity, the *Degree of Protonation*. Much like the Degree of Hydration, the Degree of Protonation is a ratio of the protonic defects versus the total number of possible defects. In this case it is the total of all protonic and electronic defects

$$X' = \frac{C_{OH_O^\bullet}}{C_{h^\bullet} + C_{OH_O^\bullet}} \quad (A.9)$$

and

$$(1 - X') = \frac{C_{h^\bullet}}{C_{h^\bullet} + C_{OH_O^\bullet}} \quad (A.10)$$

Substituting back into Equation (A.8) produces the final equation

$$j_{H_2O} = -\frac{1}{2}\frac{D_{OH_O^\bullet} D_{h^\bullet}}{X' D_{OH_O^\bullet} + (1 - X')D_{h^\bullet}}\nabla C_{OH_O^\bullet} \quad (A.11)$$

which is analogous to the Case Ia result (although involving protons and holes instead of protons and oxygen vacancies), and has similar behavior. For low degrees of protonation, $X' \to 0$, the effective flux of water becomes dependent only on the protonic diffusivity. On the other hand, as $X' \to 1$, the hole diffusivity becomes rate limiting.

It is important to note that in this case, the prefactor in eqn (A.11) cannot be construed as the effective chemical diffusivity of water. Since the water flux in this case is expressed in terms of a gradient in a charged defect species (rather than water), the equation does not directly follow Fick's First Law. It is however, possible to slightly alter eqn (A.11) to yield an alternative expression in terms of an effective hydrogen flux which does follow Fick's First Law:

$$j_{H_2} = -\frac{1}{4}\frac{D_{OH_O^\bullet} D_{h^\bullet}}{X' D_{OH_O^\bullet} + (1 - X')D_{h^\bullet}}\nabla C_{H_2} \quad (A.12)$$

Appendix B

Perhaps the biggest challenge associated with the mass balance experiments presented is interpreting the mass spectrometer data. Due to ionization fragmentation, many of the molecular species (*e.g.* H_2O, D_2O, and $H_2^{18}O$) analyzed in these experiments yield two or three distinct mass signals, and there is often duplicity in the mass of the molecules and of various fragments (*e.g.* H_2O and

DO^- both have a mass of 18 amu). Data interpretation is achieved by employing ionization probabilities to calculate the ratios of the various fragments that can be attributed to a given molecule. Those species that have fragments with unique masses (*e.g.* OH^- at 17 amu and $H_2^{18}O$ at 22 amu) are then used to deconvolute the other overlapping mass signals to determine what fraction of each signal is attributed to which species.

For cases where deconvolution is inefficient to determine a signal's origin, isotope abundance and probability is then taken into consideration. One example would be the masses of 18, 19, and 20 amu, when the ratio of D to ^{18}O is unknown in a H_2O gas stream (typically if ^{18}O containing species are not abundant enough to create a strong 21 or 22 amu signal). Since both signals could be attributed to D and ^{18}O containing species, it is helpful to look at the probability of one species to exist versus another. For the natural abundance of these isotopes it is far more likely to have an $H_2^{18}O$ (0.205% natural abundance) molecule then either a D_2O molecule or a $^{18}OD^-$ fragment, which both require the very unlikely combination of two rare isotopes (probabilities of which are $(1.15 \times 10^{-4})^2$ and $1.15 \times 10^{-4} \cdot 2.05 \times 10^{-3}$, respectively). Thus 20 amu is essentially unique to $H_2^{18}O$. Then the ionization probability for $^{18}OH^-$ can be used to determine the contribution of DOH to the 19 amu signal.

Acknowledgments

References

1 H. Iwahara, T. Esaka, H. Uchida and N. Maeda, *Solid State Ionics*, 1981, **3–4**, 359–363.
2 M. S. Lee, I. G. Koo, J. H. Kim and W. M. Lee, *Int. J. Hydrogen Energy*, 2009, **34**, 40–47.
3 H. Matsumoto, T. Shimura, H. Iwahara, T. Higuchi, K. Yashiro, A. Kaimai, T. Kawada and J. Mizusaki, *J. Alloys Compd.*, 2006, **408–412**, 456–462.
4 J. H. Tong, W. S. Yang, R. Cai, B. C. Zhu and L. W. Lin, *Catal. Lett.*, 2002, **78**, 129–137.
5 W. G. Coors, 2006.
6 N. Bonanos, *Proton Conducting Materials for Next-Generation Solid Oxide Fuel Cells*, Genoa, Italy, 2007.
7 W. G. Coors, *J. Power Sources*, 2003, **118**, 150–156.
8 K. D. Kreuer, *Annu. Rev. Mater. Res.*, 2003, **33**, 333–359.
9 H.-I. Yoo, J.-K. Kim and C.-E. Lee, *J. Electrochem. Soc.*, 2009, **156**, B66–B73.
10 H.-I. Yoo and C.-E. Lee, *Solid State Ionics*, 2009, **180**, 326–337.
11 A. Virkar, *Solid State Ionics*, 2001, **140**, 275–283.
12 K. D. Kreuer, *Solid State Ionics*, 1999, **125**, 285–302.
13 W. G. Coors and R. P. O'Hayre, CoorsTek, 2010.
14 J. Tong, D. Clark, M. Hoban and R. O'Hayre, *Solid State Ionics*, 2009.
15 K. D. Kreuer, E. Schonherr and J. Maier, *Solid State Ionics*, 1994, **70–71**, 278–284.
16 W. G. Coors, *Solid State Ionics*, 2007, **178**, 481–485.
17 W. G. Coors, *J. Electrochem. Soc.*, 2004, **151**, A994–A997.
18 T. Schober and W. G. Coors, *Solid State Ionics*, 2005, **176**, 357–362.